March 2015

Observation of antiferromagnetic correlations in the Hubbard model with ultracold atoms

Russell Hart
Rice University

Pedro Duarte
Rice University

Tsung-Lin Yang
Rice University

Xinxing Liu
Rice University

Thereza Paiva
Universidade Federal do Rio de Janeiro

See next page for additional authors

Recommended Citation

Authors

Russell Hart, Pedro Duarte, Tsung-Lin Yang, Xinxing Liu, Thereza Paiva, Ehsan Khatami, Richard Scalettar, Nandini Trivedi, David Huse, and Randall Hulet

Observation of antiferromagnetic correlations in the Hubbard model with ultracold atoms

Russell A. Hart,[1, *] Pedro M. Duarte,[1, *] Tsung-Lin Yang,[1] Xinxing Liu,[1] Thereza Paiva,[2] Ehsan Khatami,[3, 4] Richard T. Scalettar,[3] Nandini Trivedi,[5] David A. Huse,[6] and Randall G. Hulet[1, †]

[1]*Department of Physics and Astronomy and Rice Quantum Institute, Rice University, Houston, TX 77005, USA*
[2]*Instituto de Física, Universidade Federal do Rio de Janeiro Cx.P. 68.528, 21941-972 Rio de Janeiro RJ, Brazil*
[3]*Department of Physics, University of California, Davis, California 95616, USA*
[4]*Department of Physics and Astronomy, San Jose State University, San Jose, CA 95192, USA*
[5]*Department of Physics, The Ohio State University, Columbus, Ohio 43210, USA*
[6]*Department of Physics, Princeton University, Princeton, New Jersey 08544, USA*
(Dated: February 3, 2015)

Ultracold atoms in optical lattices have great potential to contribute to a better understanding of some of the most important issues in many-body physics, such as high-temperature (high-T_c) superconductivity [1]. Thirty years ago, Anderson suggested that the Hubbard model, a simplified representation of fermions moving on a periodic lattice, may contain the essence of copper oxide superconductivity [2]. The Hubbard model describes many of the features shared by the copper oxides, including an interaction-driven Mott insulating state and an antiferromagnetic (AFM) state. Optical lattices filled with a two-spin-component Fermi gas of ultracold atoms can faithfully realise the Hubbard model with readily tunable parameters, and thus provide a platform for the systematic exploration of its phase diagram [3, 4]. Realisation of strongly correlated phases, however, has been hindered by the need to cool the atoms to temperatures as low as the magnetic exchange energy, and also by the lack of reliable thermometry [5]. Here we demonstrate spin-sensitive Bragg scattering of light to measure AFM spin correlations in a realisation of the three-dimensional (3D) Hubbard model at temperatures down to 1.4 times that of the AFM phase transition. This temperature regime is beyond the range of validity of a simple high-temperature series expansion, which brings our experiment close to the limit of the capabilities of current numerical techniques. We reach these low temperatures using a unique compensated optical lattice technique [6], in which the confinement of each lattice beam is compensated by a blue-detuned laser beam. The temperature of the atoms in the lattice is deduced by comparing the light scattering to determinantal quantum Monte Carlo [7] (DQMC) and numerical linked-cluster expansion [8] (NLCE) calculations. Further refinement of the compensated lattice may produce even lower temperatures which, along with light scattering thermometry, would open avenues for achieving and characterising other novel quantum states of matter, such as the pseudogap regime of the 2D Hubbard model.

A two-spin-component Fermi gas in a simple cubic optical lattice may be described by a single-band Hubbard model with nearest-neighbour tunnelling t and on-site interaction $U > 0$. At a density n of one atom per site, and for sufficiently large U/t there is a crossover from a 'metallic' state to a Mott insulating regime [9] as the temperature T is reduced below U. The Mott regime has been demonstrated with ultracold atoms in an optical lattice by observing the reduction of doubly occupied sites [10] and the related reduction of the global compressibility [11]. For T below the Néel ordering temperature T_N, which for $U \gg t$ is approximately equal to the exchange energy $J = 4t^2/U$, the system undergoes a phase transition to an AFM state [12]. In the context of quantum simulations, AFM phases of Ising spins have been previously engineered with bosonic atoms in an optical lattice [13] and with spin-$\frac{1}{2}$ ions [14, 15]. Also, nearest-neighbour AFM correlations due to magnetic exchange have been observed along one dimension of an

anisotropic lattice [16]. The same experiment achieved temperatures as low as $T = 0.95t \simeq 2.6\,T_N$ when the lattice was configured to be isotropic [17], where $T_N = 0.36t$ is the maximal value of the Néel transition temperature [12, 18, 19].

Our experiments are performed with an all-optically produced [20], quantum degenerate, two-state mixture of the two lowest hyperfine ground states of fermionic ^{6}Li atoms, which we label $|\uparrow\rangle$ and $|\downarrow\rangle$. The repulsive interaction between atoms in states $|\uparrow\rangle$ and $|\downarrow\rangle$ is controlled via a magnetic Feshbach resonance [21], which we use to set the s-wave scattering length a_s in the range from $80\,a_0$ to $560\,a_0$, where a_0 is the Bohr radius. A simple cubic optical lattice is formed at the intersection of three mutually perpendicular infrared (IR) retroreflected laser beams. We can dynamically rotate the polarisation of the retroreflection, and thus continually adjust the potential between a lattice and a harmonic dimple trap. The overall confinement produced by the Gaussian envelope of each IR lattice beam is partially compensated with a superimposed, non-retroreflected, blue-detuned laser beam [6, 22]. The compensation beams serve three purposes: (1) They help flatten the confin-

ing potential in order to enlarge the volume of the AFM phase; (2) they provide a way to maintain the central density near $n \approx 1$ as the lattice is loaded; and (3) they may mitigate the effects of heating in the lattice by lowering the threshold for evaporation.

A degenerate sample with total atom number N between 1.0×10^5 and 2.5×10^5 is prepared in the harmonic dimple trap (without compensation) at a temperature $T/T_F = 0.04 \pm 0.02$, where T_F is the Fermi temperature. The lattice is turned on slowly to a central depth of $v_0 = 7\,E_r$ (see Methods), where $E_r = h^2/(2m\lambda^2)$ is the recoil energy, h is Planck's constant, m is the atomic mass, and $\lambda = 1,064\,$nm is the wavelength of the lattice beams. While loading the lattice, the intensities of the compensation beams are adjusted to maintain a peak density $n \simeq 1$. We have measured the temperature in the dimple trap before and after transferring the atoms to the lattice (see Methods and Extended Data Fig. 3), and have observed that the compensating beams mitigate heating in the lattice, perhaps by allowing continued evaporative cooling [6] or by a reduction of three-body loss.

Bragg scattering of near-resonant light [23–25] is depicted in Fig. 1. The Bragg condition for scattering from an AFM ordered sample is satisfied when the momentum $\boldsymbol{Q}$ transferred to a scattered photon is equal to $\boldsymbol{\pi}$, where $\boldsymbol{\pi} = \frac{2\pi}{a}(^{-1}\!/_2 \ ^{-1}\!/_2 \ ^1\!/_2)$ is a reciprocal lattice vector of the magnetic sublattice, and $a = \lambda/2$ is the lattice spacing. Cameras are positioned to detect scattering at $\boldsymbol{Q} = \boldsymbol{\pi}$ and also at $\boldsymbol{Q} = \boldsymbol{\theta}$, a momentum transfer that does not satisfy the Bragg condition and is used as a control. We obtain spin sensitivity, in analogy to neutron scattering in condensed matter, by setting the Bragg laser frequency between the optical transition frequencies for the two spin states [26, 27]. Prior to the measurement, we jump v_0 to $20\,E_r$ in a few μs to lock the atoms in place (see Methods), and then illuminate them *in-situ* for 1.7μs with the Bragg probe. Alternatively, we can suddenly turn off the $20\,E_r$ lattice and illuminate the atoms after time-of-flight τ.

Figure 2 shows the results of simultaneous measurements of the scattered intensity for $\boldsymbol{Q} = \boldsymbol{\pi}$ and $\boldsymbol{Q} = \boldsymbol{\theta}$ ($I_{\boldsymbol{\pi}}$ and $I_{\boldsymbol{\theta}}$, respectively), as a function of τ. After a few μs of expansion, when the extent of the atomic wavepackets becomes comparable to the lattice spacing, the light scattered from correlated spins no longer interferes constructively at the detector. More precisely, the Debye-Waller factor $e^{-2W_{\boldsymbol{Q}}(\tau)} = \exp\left[-\sum_{i=x,y,z} Q_i^2 \langle r_i^2 \rangle_\tau\right]$ decays to zero after a sufficiently long τ (see Methods) and the sample is effectively uncorrelated. Here r_i is the displacement of an atom from the centre of the lattice site at which it was initially localised.

By comparing the intensity of the light scattered *in-situ* ($\tau = 0$) to that after sufficiently long τ ($I_{\boldsymbol{Q}0}$ and $I_{\boldsymbol{Q}\infty}$, respectively), we effectively normalise the Bragg scattering signal to the diffuse scattering background
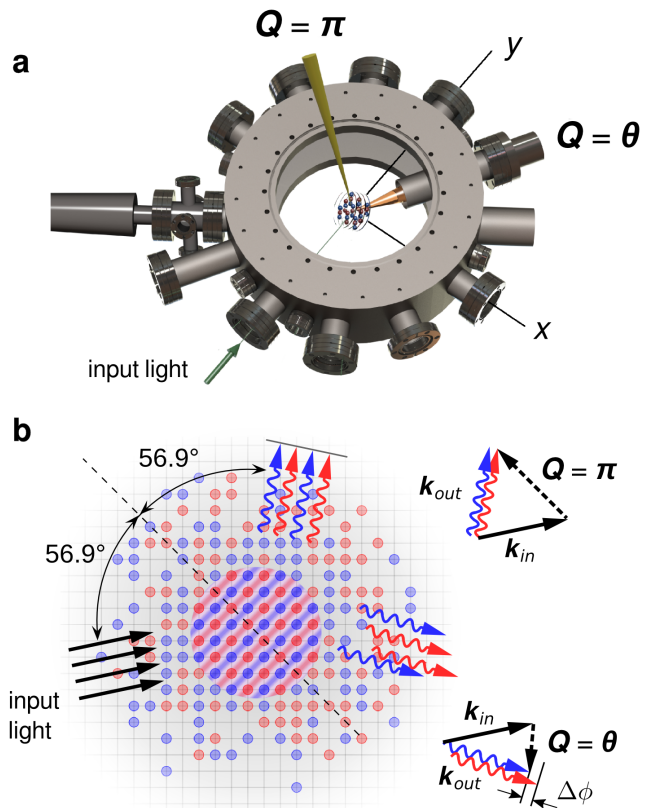

FIG. 1. **Schematic depiction of Bragg scattering. a**, Rendering of the experimental setup used for Bragg scattering. Light is collected for momentum transfers $\boldsymbol{Q} = \boldsymbol{\pi}$ and $\boldsymbol{Q} = \boldsymbol{\theta}$. A bias magnetic field, which sets the quantisation axis and the interaction strength, points in the z direction. The input Bragg beam lies in the yz plane, and its wavevector makes an angle of $3°$ with the positive y axis. **b**, The two spin states are denoted by red and blue circles. AFM order develops at the Mott plateau, shown here to be located in the centre, where $n \simeq 1$. AFM correlations are suppressed outside the central region where $n < 1$. Bragg scattering requires the input and output wavevectors, $\boldsymbol{k}_{in}$ and $\boldsymbol{k}_{out}$, respectively, to satisfy the Bragg condition $\boldsymbol{k}_{out} - \boldsymbol{k}_{in} = \boldsymbol{\pi}$. The red and blue arrows denote light scattered from one spin state or the other. The two spin states scatter with opposite phase shift, so that their respective sublattices interfere constructively for $\boldsymbol{Q} = \boldsymbol{\pi}$. For a different momentum transfer $\boldsymbol{k}_{out} - \boldsymbol{k}_{in} = \boldsymbol{\theta}$, scattering is relatively insensitive to AFM correlations due to the lack of constructive interference between the scattered photons, which have random relative phases $\Delta\phi$.

of an uncorrelated sample, achieving high sensitivity to magnetic ordering and strong rejection of common mode systematics. Figure 2 shows that there is enhanced scattering at $\tau = 0$ relative to the uncorrelated cloud ($\tau = 9\,\mu$s) for $\boldsymbol{Q} = \boldsymbol{\pi}$, whereas for $\boldsymbol{Q} = \boldsymbol{\theta}$ scattering at $\tau = 0$ is reduced, such that $I_{\boldsymbol{\theta}0}/I_{\boldsymbol{\theta}\infty} < 1$. Double occupancies, present as 'virtual' states even at low temperatures [28], reduce coherent scattering in all directions, since each atom in the pair has opposite spin and there-
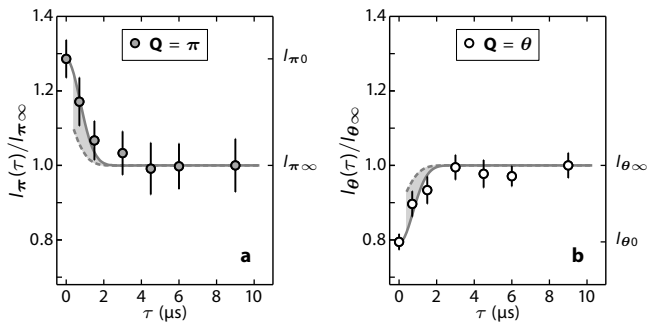
FIG. 2. **Time-of-flight measurement of scattered intensity from a sample with AFM correlations. a,** Normalised intensity of Bragg scattered light ($\boldsymbol{Q} = \boldsymbol{\pi}$) as a function of time-of-flight τ. The *in-situ* ($\tau = 0$) scattered intensity is denoted as $I_{\boldsymbol{Q}0}$, while the intensity after sufficiently long τ, corresponding to an effectively uncorrelated sample, is denoted as $I_{\boldsymbol{Q}\infty}$. **b,** For $\boldsymbol{Q} = \boldsymbol{\theta}$ the *in-situ* sample shows a reduction of scattering, as compared to long τ, due to the presence of double occupancies and to the presence of AFM spin correlations (see text). Each data point and error bar is the mean and standard error of the mean (s.e.m.) of at least 17 measurements of the scattered intensity. The grey solid line is the intensity calculated using the value of the Debye-Waller factor at τ, whereas the dashed grey line uses the average value of the Debye-Waller factor during the $1.7\,\mu s$ exposure of the Bragg probe (see text and Methods).

fore scatters with opposite phase. For $\boldsymbol{Q} = \boldsymbol{\pi}$ the coherent enhancement from AFM spin correlations exceeds this reduction. Furthermore, the coherent enhancement of the signal along $\boldsymbol{Q} = \boldsymbol{\pi}$ suppresses the scattered intensity in other directions.

For a momentum transfer $\boldsymbol{Q}$, the spin structure factor $S_{\boldsymbol{Q}}$ of the sample is defined as

$$S_{\boldsymbol{Q}} \equiv \frac{4}{N} \sum_{i,j} e^{i\boldsymbol{Q}\cdot(\boldsymbol{R}_i - \boldsymbol{R}_j)} \langle \sigma_{zi}\sigma_{zj} \rangle \qquad (1)$$

Here N is the total number of atoms, the sums extend over all lattice sites i and j, $\boldsymbol{R}_j$ is the location of the jth site, and σ_{zj} is the z component of the spin operator for the jth site:

$$\sigma_{zj}|0\rangle_j = 0|0\rangle_j \qquad \sigma_{zj}|{\uparrow}\rangle_j = +\frac{1}{2}|{\uparrow}\rangle_j$$

$$\sigma_{zj}|{\downarrow}\rangle_j = -\frac{1}{2}|{\downarrow}\rangle_j \qquad \sigma_{zj}|{\uparrow\downarrow}\rangle_j = 0|{\uparrow\downarrow}\rangle_j$$

In a sample with complete AFM ordering $S_{\boldsymbol{\pi}} \simeq N$, whereas for uncorrelated samples in the lattice $S_{\boldsymbol{\pi}} \leq 1$ and $S_{\boldsymbol{\theta}} \leq 1$. The choice of the z spin component for this analysis is arbitrary, as each of the other axes would result in the same value for $S_{\boldsymbol{Q}}$ in the absence of a symmetry-breaking field. In the limit of tightly localised wavefunctions ($e^{-2W_{\boldsymbol{Q}}(\tau=0)} \approx 1$), and for a weak probe, the spin structure factor is $S_{\boldsymbol{Q}} \approx I_{\boldsymbol{Q}0}/I_{\boldsymbol{Q}\infty}$. We determine the spin structure factor by measuring the scattered
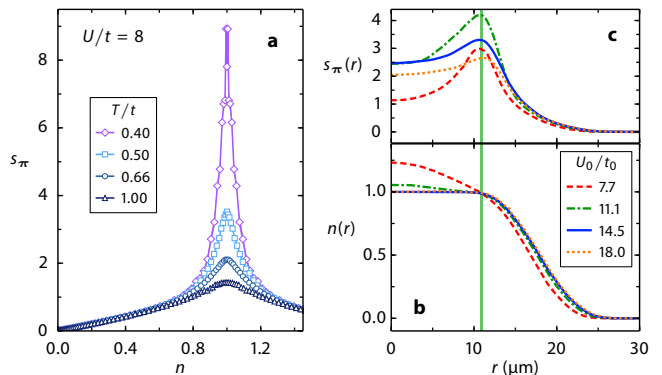
FIG. 3. **Numerical calculations a,** Spin structure factor per lattice site $s_{\boldsymbol{\pi}}$ as a function of n in a homogeneous lattice for several temperatures (see Methods). $s_{\boldsymbol{\pi}}$ is sharply peaked near $n = 1$ and diverges as T approaches T_N. **b,** Density profiles calculated at $T/t_0 = 0.6$ for different U_0/t_0, using in each case the value of N that maximises the experimentally measured $S_{\boldsymbol{\pi}}$ (see text and Extended Data Fig. 2.) **c,** Profiles of the local spin structure factor $s_{\boldsymbol{\pi}}(r)$, for the same conditions as in **b**. The vertical green line in panels **b** and **c** marks the radius at which $s_{\boldsymbol{\pi}}(r)$ is maximised for $U_0/t_0 = 11.1$ (see text).

intensities $I_{\boldsymbol{Q}0}$ and $I_{\boldsymbol{Q}\infty}$ and applying a correction to account for the *in-situ* Debye-Waller factor in the $20\,E_r$ lattice and for saturation of the atomic transition, which generates a small component of inelastically scattered light (see Methods).

Within the local density approximation (LDA) we model the sample by considering each point in the trap as a homogeneous system in equilibrium at a temperature T, with local values of the chemical potential and the Hubbard parameters determined by the trap potential. The spin structure factor of the sample $S_{\boldsymbol{Q}}$ can then be expressed as the integral over the trap of the local spin structure factor per lattice site, $s_{\boldsymbol{Q}}$. Figure 3a shows numerical calculations of $s_{\boldsymbol{\pi}}$ for various temperatures in a homogeneous lattice with $U/t = 8$, close to where T_N is maximal [12]. The figure shows that $s_{\boldsymbol{\pi}}$ is sharply peaked around $n = 1$ and grows rapidly as T approaches T_N from above.

Figures 3b and 3c show n and $s_{\boldsymbol{\pi}}$ profiles, respectively, calculated for our experimental parameters at various values of U_0/t_0, where U_0 and t_0 denote the local values of the Hubbard parameters at the centre of the trap. As seen in Fig. 3b, only a fraction of the atoms in the sample is near $n = 1$, where AFM correlations are maximal. The finite extent of the lattice beams causes the lattice depth to decrease with distance from the centre, resulting in an increasing t such that both U/t and T/t decrease with increasing radius for constant T (see Extended Data Fig. 1). The radial decrease in T/t causes $s_{\boldsymbol{\pi}}(r)$ to maximise at the largest radius for which the density is $n \approx 1$. For large U_0/t_0 the cloud exhibits an $n = 1$

Mott plateau and $s_{\boldsymbol{\pi}}(r)$ is maximised at the outermost radius of the plateau.

In the experiment, we measure $S_{\boldsymbol{Q}}$ as a function of U_0/t_0. At each value of U_0/t_0 we vary the atom number N to maximise the measured $S_{\boldsymbol{\pi}}$ (see Methods and Extended Data Fig. 2). According to the picture presented above, this has the effect of optimising the size and location of the $n = 1$ region of the cloud such that AFM correlations are maximised. The compensation strength g_0, which is the same for all U_0/t_0, was also adjusted to maximise $S_{\boldsymbol{\pi}}$. We found the optimum to be $g_0 = 3.7\,E_r$ at a lattice depth $v_0 = 7\,E_r$ (see Methods). Besides the equilibrium considerations regarding the optimal size and location of the Mott plateau, we believe that the dynamical adjustment of g_0 during the lattice turn-on reduces the time for the system to equilibrate, by minimising the deviation of the equilibrium density distribution in the final potential from the starting density distribution in the dimple trap prior to loading the lattice.

Figure 4 shows the measured values of $S_{\boldsymbol{\pi}}$ and $S_{\boldsymbol{\theta}}$ at optimal N for various values of U_0/t_0 (see Extended Data Fig. 5 for the raw counts at the CCD cameras). We find that $S_{\boldsymbol{\pi}}$ is peaked for $11 < U_0/t_0 < 15$. In contrast, the measurements of $S_{\boldsymbol{\theta}}$ vary little over the range of interaction strengths, consistent with an absence of coherent Bragg scattering in this direction. Measurements of $S_{\boldsymbol{\pi}}$ after hold time in the lattice show that the Bragg signal decays for larger temperatures (see Extended Data Fig. 4). Comparing the measured $S_{\boldsymbol{\pi}}$ with numerical calculations for a homogeneous lattice (for example, those in Fig. 3a) allows us to set a trap independent upper limit on the temperature, which we determine to be $T/t_0 < 0.7$.

Precise thermometry is obtained by comparing the measured $S_{\boldsymbol{\pi}}$ with numerical calculations averaged over the trap density distribution for different values of T. The results of such numerical calculations are shown in Fig. 4, labelled by the value of T/t_*, which we define as the local value of T/t at the radius where the spin structure factor per lattice site is maximal (see Fig. 3c). At $U_0/t_0 = 11.1$, where measured AFM correlations are maximal, we find $T/t_* = 0.51 \pm 0.06$, where the uncertainty is due to the statistical error in the measured $S_{\boldsymbol{\pi}}$ and the systematic uncertainty in the lattice parameters used for the numerical calculation. This temperature is consistent with the data at all values of U_0/t_0. We caution, however, that for values of $U/t > 10$ a single-band Hubbard model may not be adequate, as corrections involving higher bands may become non-negligible [27, 29].

As was shown in Fig. 3b, for $U_0/t_0 = 11.1$ the dominant contribution to $S_{\boldsymbol{\pi}}$ comes from the outermost radius of the Mott plateau. At that radius, the local value of U/t is $U_*/t_* = 9.1$, consistent with DQMC calculations for the homogeneous lattice [12, 18, 19], which find T_N to be maximised for U/t between 8 and 9. For $U_0/t_0 = 11.1$, $t_* = 1.3\,\mathrm{kHz}$, so we can infer the temperature of the system to be $T = 32 \pm 4\,\mathrm{nK}$. In terms of T_N, the tem-
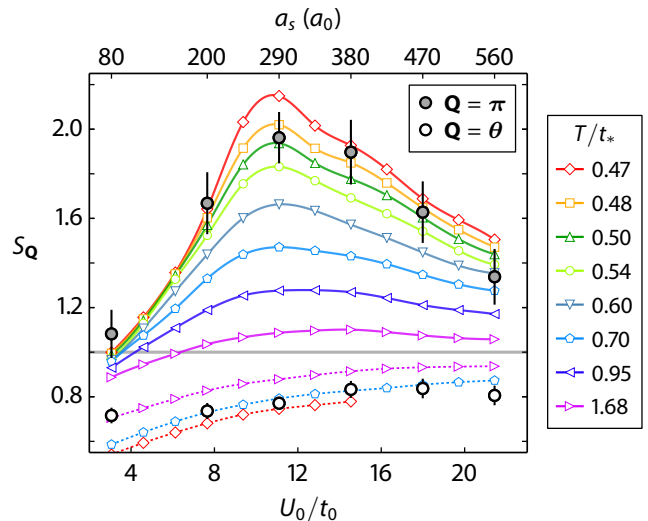
FIG. 4. **Spin structure factor** Measured $S_{\boldsymbol{\pi}}$ (filled circles) and $S_{\boldsymbol{\theta}}$ (open circles) at optimised N (see text) for various U_0/t_0. The values of the s-wave scattering length corresponding to U_0/t_0 for the experimental points are shown along the top axis. For each point at least 40 *in-situ* and 40 time-of-flight measurements of the scattered intensities are used to obtain the spin structure factor. Error bars are obtained from the s.e.m. of the scattered intensities; the raw data is presented in Extended Data Fig. 5. Numerical calculations of $S_{\boldsymbol{\pi}}$ (open symbols, lines as guide to the eye) and $S_{\boldsymbol{\theta}}$ (open symbols, dashed lines as guide to the eye) for various values of T/t_*. The numerical calculations for $S_{\boldsymbol{\theta}}$ are unreliable for $T/t_* < 0.7$ and $U_0/t_0 > 15$. $S_{\boldsymbol{\theta}}$ decreases slightly for weak interactions, where the fraction of double occupancies increases.

perature is $T/T_N = 1.42 \pm 0.16$. At this temperature, the numerical calculations indicate that the correlation length is approximately the lattice spacing. The calculations show that the entropy per particle in the trap is $S/(Nk_{\mathrm{B}}) \simeq 0.43$, where k_{B} is the Boltzmann constant (see Extended Data Fig. 6). This entropy range is consistent with $T/T_F = 0.04 \pm 0.02$ measured in the harmonic dimple trap before loading the atoms into the lattice [30], and thus justifies the assumption of adiabatic loading.

In conclusion, we have observed AFM correlations in the 3D Hubbard model using ultracold atoms in an optical lattice via spin-sensitive Bragg scattering of light. Because magnetic order is extremely sensitive to T in the vicinity of T_N, Bragg scattering provides precise thermometry in regimes previously inaccessible to quantitative temperature measurements. While previous cold atom experiments on the 3D Fermi-Hubbard model were in a temperature regime that could be accurately represented by a simple high-temperature series expansion, the data presented here is near the limit of the capabilities of advanced numerical simulations. Our experimental setup can be configured to study the 2D Hubbard model in an array of planes; further progress to lower temperature will put us in a position to answer questions about com-

peting pairing mechanisms in 2D, and may ultimately resolve the long standing question of d-wave superconductivity in the Hubbard model.

---

[1] W. Hofstetter, J. I. Cirac, P. Zoller, E. Demler, and M. D. Lukin, Phys. Rev. Lett. **89**, 220407 (2002).
[2] P. W. Anderson, Science **235**, 1196 (1987).
[3] D. Jaksch and P. Zoller, Annals of Physics **315**, 52 (2005), special Issue.
[4] I. Bloch, J. Dalibard, and W. Zwerger, Rev. Mod. Phys. **80**, 885 (2008).
[5] D. C. McKay and B. DeMarco, Reports on Progress in Physics **74**, 054401 (2011).
[6] C. J. M. Mathy, D. A. Huse, and R. G. Hulet, Phys. Rev. A **86**, 023606 (2012).
[7] R. Blankenbecler, D. J. Scalapino, and R. L. Sugar, Phys. Rev. D **24**, 2278 (1981).
[8] M. Rigol, T. Bryant, and R. R. P. Singh, Phys. Rev. Lett. **97**, 187202 (2006).
[9] M. Imada, A. Fujimori, and Y. Tokura, Rev. Mod. Phys. **70**, 1039 (1998).
[10] R. Jördens, N. Strohmaier, K. Günter, H. Moritz, and T. Esslinger, Nature **455**, 204 (2008).
[11] U. Schneider, L. Hackermller, S. Will, T. Best, I. Bloch, T. A. Costi, R. W. Helmes, D. Rasch, and A. Rosch, Science **322**, 1520 (2008).
[12] R. Staudt, M. Dzierzawa, and A. Muramatsu, The European Physical Journal B - Condensed Matter and Complex Systems **17**, 411 (2000).
[13] J. Simon, W. S. Bakr, R. Ma, M. E. Tai, P. M. Preiss, and M. Greiner, Nature **472**, 307 (2011).
[14] K. Kim, M.-S. Chang, S. Korenblit, R. Islam, E. Edwards, J. Freericks, G.-D. Lin, L.-M. Duan, and C. Monroe, Nature **465**, 590 (2010).
[15] J. W. Britton, B. C. Sawyer, A. C. Keith, C.-C. J. Wang, J. K. Freericks, H. Uys, M. J. Biercuk, and J. J. Bollinger, Nature **484**, 489 (2012).
[16] D. Greif, T. Uehlinger, G. Jotzu, L. Tarruell, and T. Esslinger, Science **340**, 1307 (2013).
[17] J. Imriška, M. Iazzi, L. Wang, E. Gull, D. Greif, T. Uehlinger, G. Jotzu, L. Tarruell, T. Esslinger, and M. Troyer, Phys. Rev. Lett. **112**, 115301 (2014).
[18] T. Paiva, Y. L. Loh, M. Randeria, R. T. Scalettar, and N. Trivedi, Phys. Rev. Lett. **107**, 086401 (2011).
[19] E. Kozik, E. Burovski, V. W. Scarola, and M. Troyer, Phys. Rev. B **87**, 205102 (2013).
[20] P. M. Duarte, R. A. Hart, J. M. Hitchcock, T. A. Corcovilos, T.-L. Yang, A. Reed, and R. G. Hulet, Phys. Rev. A **84**, 061406 (2011).
[21] M. Houbiers, H. T. C. Stoof, W. I. McAlexander, and R. G. Hulet, Phys. Rev. A **57**, R1497 (1998).
[22] P. N. Ma, K. Y. Yang, L. Pollet, J. V. Porto, M. Troyer, and F. C. Zhang, Phys. Rev. A **78**, 023605 (2008).
[23] G. Birkl, M. Gatzke, I. H. Deutsch, S. L. Rolston, and W. D. Phillips, Phys. Rev. Lett. **75**, 2823 (1995).
[24] M. Weidemüller, A. Görlitz, T. W. Hänsch, and A. Hemmerich, Phys. Rev. A **58**, 4647 (1998).
[25] H. Miyake, G. A. Siviloglou, G. Puentes, D. E. Pritchard, W. Ketterle, and D. M. Weld, Phys. Rev. Lett. **107**, 175302 (2011).
[26] T. A. Corcovilos, S. K. Baur, J. M. Hitchcock, E. J. Mueller, and R. G. Hulet, Phys. Rev. A **81**, 013415 (2010).
[27] F. Werner, O. Parcollet, A. Georges, and S. R. Hassan, Phys. Rev. Lett. **95**, 056401 (2005).
[28] S. Fuchs, E. Gull, L. Pollet, E. Burovski, E. Kozik, T. Pruschke, and M. Troyer, Phys. Rev. Lett. **106**, 030401 (2011).
[29] C. J. M. Mathy and D. A. Huse, Phys. Rev. A **79**, 063412 (2009).
[30] M. Köhl, Physical Review A **73**, 031601 (2006).

ACKNOWLEDGEMENTS

AUTHOR CONTRIBUTIONS

The experimental work was performed by R.A.H., P.M.D., T.-L.Y., X.L., and R.G.H., while T.P., E.K., P.M.D., R.T.S., N.T., and D.A.H. performed the theory needed to extract temperatures from the data and provided overall theoretical guidance. All authors contributed to the writing of the manuscript.

METHODS

Preparation.

^{6}Li atoms are first captured and cooled in a magneto-optical trap (MOT) operating at 671 nm. They are further cooled in a second MOT stage employing 323 nm light near resonant with the $2S \to 3P$ transition. As described previously [20], these atoms are laser cooled into a large volume optical dipole trap (ODT) where a balanced spin mixture of the states $|\uparrow\rangle = |2S_{1/2}; F = 1/2, m_F = +1/2\rangle$ and $|\downarrow\rangle = |2S_{1/2}; F = 1/2, m_F = -1/2\rangle$ is produced.

Once the large volume ODT is loaded, we set the magnetic field to 340 G ($a_s \simeq -289 \, a_0$) to perform evaporative cooling. The intensities of the lattice beams (1,064 nm) in dimple configuration (with the polarisation of each retroreflection perpendicular to that of each input beam) are turned on in 1 s. The depth of the dimple, which at this point is only a small perturbation on the ODT, is adjusted to control the final atom number in the experiment. The depth of the ODT is then

ramped to zero in 5.5 s to evaporatively cool the atoms into the dimple. To produce a final sample with repulsive interactions, the magnetic field is increased to 595 G ($a_s \simeq 326\, a_0$) in a 5 ms linear ramp starting 3 s into the evaporation trajectory. Due to the small volume of the dimple relative to the ODT, evaporation into the dimple is efficient and deeply degenerate samples are reliably produced.

We measure T/T_F in the dimple trap by fitting the density profile, after 0.5 ms of time-of-flight, to a Thomas-Fermi distribution [31]. The magnetic field is tuned to 528 G to make the gas non-interacting prior to the measurement. For the experiments reported here, the final dimple depths are in the range between $0.325\, E_r$ and $0.5\, E_r$ per axis, resulting in N between $1.0-2.5\times10^5$. The measured value $T/T_F = 0.04 \pm 0.02$ is independent of N within this range. The uncertainty in T/T_F is the standard deviation of the fitted value for at least six independent realisations.

Compensated optical lattice.

The experiment takes place in a compensated simple cubic optical lattice potential that can be expressed as

$$V_{3D}(x,y,z) = V_{1D}(x;y,z) + V_{1D}(y;z,x) + V_{1D}(z;x,y),$$

where

$$V_{1D}(x;y,z) = V_L(x;y,z) + V_C(x;y,z),$$

and V_L, V_C are the potentials produced by the lattice (1,064 nm) and compensation (532 nm) beams respectively:

$$V_L(x;y,z) = -v_0 \exp\left[-2\frac{y^2 + z^2}{w_L^2}\right] \cos^2(\frac{2\pi}{\lambda}x)$$

$$V_C(x;y,z) = g_0 \exp\left[-2\frac{y^2 + z^2}{w_C^2}\right].$$

Here, v_0 is the lattice depth and g_0 is the compensation ($v_0, g_0 > 0$). A schematic of the compensated lattice, and the spatial variation of the Hubbard parameters due to the finite lattice beam waists, are shown in Extended Data Fig. 1.

The beam waists ($1/e^2$ radius) of the three axes are calibrated independently by phase modulation spectroscopy of each lattice beam and by measuring the frequency of breathing mode oscillations. The waists are found to be (up to a $\pm5\%$ systematic uncertainty) $w_L = (47, 47, 44)\, \mu$m and $w_C = (42, 41, 40)\, \mu$m, for beams propagating along x, y, z, respectively.

Lattice loading.

To load the lattice from the dimple trap we first rotate the polarisation of the retroreflected beams parallel to that of the input beams in 100 ms. In the following 25 ms, we increase the lattice depth to $2.5\, E_r$ and ramp the magnetic field to set the final value of U_0/t_0. The lattice depth is then ramped to $7.0\, E_r$ in 15 ms.

Throughout the process of loading the lattice from the dimple, the power of the compensating beams is adjusted in order to maintain the peak density of the sample at $n \simeq 1$. At the final lattice depth of $v_0 = 7.0\, E_r$, the average compensation per beam is $g_0 = 3.7\, E_r$. The value of g_0 for each beam is adjusted slightly from this average in order to create samples that appear spherically symmetric.

Round-trip T/T_F measurements.

After loading the atoms into the $7E_r$ lattice we wait for a hold time t_h and then reverse the lattice loading ramps to return to the harmonic dimple trap and measure T/T_F. This measurement, shown in Extended Data Fig. 3, sets an upper limit on the entropy of the system in the lattice, and is also a measure of the heating rate of the system in the lattice.

Temperature dependence of S_π

In Extended Data Fig. 4 we show S_π as a function of hold time in the lattice t_h and observe that it decays for longer hold times, as expected from the increase in T/T_F. Although the preparation of the sample and the final potential are somewhat different for the data presented in Extended Data Figs. 3 and 4, the data support the contention that the Bragg signal decreases with increasing T.

Variation of N to maximise S_π.

The global chemical potential μ_0 must be increased for larger U_0/t_0 to guarantee the formation of a Mott plateau in the trap. A larger μ_0 results in larger atom number. N is adjusted to maximise the Bragg signal for each experimental value of U_0/t_0 in Fig. 4. We adjust N by tuning the depth of the dimple trap in which degeneracy is achieved prior to loading the atoms into the lattice. The optimal value of N as a function of U_0/t_0 is shown in Extended Data Fig. 2.

Spin structure factor measurement.

We measure the spin structure factor at two different values of the momentum transfer $\boldsymbol{Q}$ given by

$$\boldsymbol{\pi} = \frac{2\pi}{a}(-0.5, -0.5, +0.5)$$

$$\boldsymbol{\theta} = \frac{2\pi}{a}(+0.396, -0.105, -0.041),$$

where $a = \lambda/2$ is the lattice spacing.

We detect the scattered light using two separate cameras as the cloud is illuminated with the Bragg probe beam for $1.7\,\mu s$. The Bragg probe beam is a collimated Gaussian beam with a waist of $450\,\mu m$ and $250\,\mu W$ of power, resulting in an intensity $I_p = 79\,\text{mW/cm}^2$. The intensity of the probe determines the on-resonance saturation parameter $s_0 = I_p|\hat{\boldsymbol{e}}_p \cdot \hat{\boldsymbol{e}}_{-1}|^2 / \left(\frac{\pi hc\Gamma}{3\lambda_0^3}\right) = 15.5$, where c is the speed of light, $\hat{\boldsymbol{e}}_p$ is the polarisation of the probe light, $\hat{\boldsymbol{e}}_{-1}$ is the unit vector in the direction of the dipole matrix element of the transition, $\lambda_0 = 671\,\text{nm}$ is the wavelength of the transition, and Γ is its linewidth. The polarisation of the incident light in our experiment is linear and perpendicular to the quantisation axis, so $|\hat{\boldsymbol{e}}_p \cdot \hat{\boldsymbol{e}}_{-1}|^2 = 1/2$. The Bragg probe detuning is set between the two spin states, such that $\Delta = |\Delta_\uparrow| = |\Delta_\downarrow| = 6.4\Gamma$, where $\Delta_\uparrow$ and $\Delta_\downarrow$ are the detunings from the two spin states.

The spin structure factor is defined in equation (1) as a sum over lattice sites i, j. By quickly ramping the lattice depth to $v_0 = 20\,E_r$, the state of the system is projected into a product state, where the wavefunction of each atom is localised at a lattice site. Hence, we can write $S_{\boldsymbol{Q}}$ as a sum over particles m, n:

$$S_{\boldsymbol{Q}} = \frac{4}{N} \sum_{m,n} e^{i\boldsymbol{Q}\cdot(\boldsymbol{R}_m - \boldsymbol{R}_n)} \langle\sigma_z\rangle_m \langle\sigma_z\rangle_n$$

where $\langle\sigma_z\rangle_n$ is the z component of the spin of the nth atom.

When illuminated with the probe light, each atom can be considered as an independent scatterer, and the intensity at the detector can be obtained by summing the field contributions from the individual atoms and squaring the total field. We assume that the spatial wavefunction of all atoms is the harmonic oscillator ground state in a lattice site of depth v_0, and that it does not change during the measurement. The resulting intensity at the detector is given by

$$I_{\boldsymbol{Q}}(\tau) = \frac{As_0/2}{4\delta^2 + s_0} N$$
$$+ e^{-2W_{\boldsymbol{Q}}(\tau)} \frac{2As_0\delta^2}{(4\delta^2 + s_0)^2} \sum_{\substack{m,n \\ m\neq n}} 4\langle\sigma_z\rangle_m \langle\sigma_z\rangle_n e^{i\boldsymbol{Q}\cdot(\boldsymbol{R}_n - \boldsymbol{R}_m)}$$

$$(2)$$

where $\delta = \Delta/\Gamma$, and $A = \frac{3}{8\pi} \frac{\hbar ck\Gamma}{r_D^2}|\boldsymbol{\Lambda}|^2$. Here $\boldsymbol{\Lambda}$ is the polarisation vector of the scattered field, $\boldsymbol{\Lambda} = \hat{\boldsymbol{n}} \times (\hat{\boldsymbol{n}} \times \hat{\boldsymbol{e}}_{-1})$, where $\hat{\boldsymbol{n}}$ is a unit vector pointing in the direction of the detector.

In equation (2) the first term arises from uncorrelated scattering by the atoms, while the second term represents the interference due to magnetic correlations. We can identify the spin structure factor in the interference term as

$$\sum_{\substack{m,n \\ m\neq n}} 4\langle\sigma_z\rangle_m \langle\sigma_z\rangle_n e^{i\boldsymbol{Q}\cdot(\boldsymbol{R}_n - \boldsymbol{R}_m)} = N(S_{\boldsymbol{Q}} - 1)$$

and obtain

$$S_{\boldsymbol{Q}} = 1 + C_{\boldsymbol{Q}}(\tau)\left(\frac{I_{\boldsymbol{Q}}(\tau)}{I_{\boldsymbol{Q}\infty}} - 1\right)$$

where $I_{\boldsymbol{Q}\infty} = \frac{As_0/2}{4\delta^2 + s_0}N$, and the correction factor is $C_{\boldsymbol{Q}}(\tau) = e^{2W_{\boldsymbol{Q}}(\tau)}(1 + \frac{s_0}{4\delta^2})$. In the experiment we obtain $S_{\boldsymbol{Q}}$ by combining measurements of the scattered intensity *in-situ* ($\tau = 0$) and after sufficiently long time-of-flight ($\tau = 6\,\mu s$). The correction factor takes the values $C_{\boldsymbol{\pi}}(\tau = 0) = 1.52$ for $\boldsymbol{Q} = \boldsymbol{\pi}$ and $C_{\boldsymbol{\theta}}(\tau = 0) = 1.18$ for $\boldsymbol{Q} = \boldsymbol{\theta}$.

Time-of-flight.

After the atoms are released in time-of-flight, the Debye-Waller factor decays as the atomic wavefunctions expand, resulting in a corresponding decay of the Bragg scattered intensity. For a lattice of depth v_0

$$e^{-2W_{\boldsymbol{Q}}(\tau)} = e^{-2W_{\boldsymbol{Q}}(\tau=0)} \exp\left[-\frac{\sqrt{v_0/E_r}}{2}\left(\frac{|\boldsymbol{Q}|h}{2ma}\right)^2 \tau^2\right].$$

This equation was used to calculate the solid grey line in Fig. 2. The average value of the Debye-Waller factor during the duration of the Bragg exposure

$$(1.7\,\mu s)^{-1} \int_\tau^{\tau + 1.7\,\mu s} e^{-2W_{\boldsymbol{Q}}(\tau')} d\tau'$$

is used to calculate the dashed grey line in Fig. 2.

The data shown in Fig. 2 was taken at $U_0/t_0 = 13.4$ with $N = 2.5 \times 10^5$ atoms. This value of N is above the optimal value, so the ratio of $I_{\boldsymbol{\pi}0}/I_{\boldsymbol{\pi}\infty}$ in Fig. 2 gives $S_{\boldsymbol{\pi}} \simeq 1.4$, which is less than the expected optimal value of $S_{\boldsymbol{\pi}}$ from Fig. 4.

Momentum transferred from the probe to the atoms.

As mentioned above, we assume that the spatial wavefunction of the atoms remains unchanged for the duration of the exposure. For this assumption to be valid,

the Lamb-Dicke parameter $\eta^2 = \frac{h^2/(2m\lambda_0^2)}{2E_r\sqrt{v_0/E_r}}$ needs to be $\ll 1$. In the $20\,E_r$ lattice, $\eta^2 = 0.27$, meaning that approximately one out of every 4 photons scattered will excite an atom to the second band of the lattice. An atom in the second band has larger position uncertainty and hence a smaller Debye-Waller factor, which reduces its contribution to the Bragg scattering signal.

The total number of photons scattered per atom is given by $N_{\rm p} = t_{\rm exp}\Gamma\frac{s_0/2}{s_0+4\delta^2}$, where the duration of the probe is $t_{\rm exp} = 1.7\,\mu$s. For $s_0 = 15.5$ and $\delta = 6.4$, $N_{\rm p} = 2.7$, thus justifying the assumption that the atoms remain in the lowest band during the pulse.

For the Bragg scattering measurements performed after time-of-flight, the momentum transferred from the probe to the atoms plays a more significant role, since the atoms are not trapped and will recoil after every photon scatter. Despite this, we still see a good agreement between the observed decay of the Bragg scattering signal and the decay expected for a Heisenberg limited wavepacket, as shown in Fig. 1. We have also performed non-spin-sensitive Bragg scattering measurements from the 010 planes of the lattice and observe the same agreement, justifying that momentum transfer from the probe to the atoms can be neglected for the exposure times used.

Optical density.

A low optical density of the sample is important so that the probe is unattenuated through the atom cloud, and multiple scattering events of the Bragg scattered photons are limited [26]. The optical density can be approximated as

$$\text{OD} \simeq \frac{\sigma_0|\hat{\boldsymbol{e}}_{\rm p}\cdot\hat{\boldsymbol{e}}_{-1}|^2}{4\delta^2+s_0}\frac{1}{a^2}\left(\frac{3N}{4\pi}\right)^{1/3}$$

where $\sigma_0 = 3\lambda_0^2/2\pi$. With $s_0 = 15.5$, $\delta = 6.4$ and $N = 1.8\times10^5$ atoms we have $\text{OD} \simeq 0.072$. At this value we do not expect significant corrections to the spin structure factor measurement due to the attenuation of the probe. We have not included any corrections in our measurement due to finite optical density effects.

Light collection.

We collect Bragg scattered light in the $\boldsymbol{\pi}$ direction over a full angular width of 110 mrad, given by a 2.5 cm diameter collection lens located 23 cm away from the atoms. In the $\boldsymbol{\theta}$ direction, light is collected by a 2.5 cm diameter lens placed 8 cm away from the atoms, corresponding to a full angular width of 318 mrad. The scattered light in each of the directions is focused to a few pixels on

the cameras, so no additional angular information is obtained. For $N = 1.8\times10^5$, $s_0 = 15.5$, $\Delta = 6.4\,\Gamma$ and a $1.7\,\mu$s pulse, the detector in the $\boldsymbol{\pi}$ direction collects approximately 1300 photons, whereas the detector in the $\boldsymbol{\theta}$ direction collects approximately 10^4 photons. The noise floor from readout, dark current and background light per shot has a variance equivalent to approximately 250 photons in the $\boldsymbol{\pi}$ direction and 1000 photons in the $\boldsymbol{\theta}$ direction.

Data averaging.

The signals we detect are small enough that an uncorrelated sample may, in a single shot, produce a scattering signal as large as the ones produced by samples with AFM correlations. To obtain a reliable measurement of $S_{\boldsymbol{\pi}}$ we average at least 40 in-situ shots to obtain $I_{\boldsymbol{Q}0}$ and at least 40 time-of-flight shots to obtain $I_{\boldsymbol{Q}\infty}$.

We estimate the expected variance on $S_{\boldsymbol{\pi}}$ by considering a randomly ordered sample in which $e^{i\boldsymbol{\pi}\cdot\boldsymbol{R}_n}2\langle\sigma_z\rangle_n$ is equal to +1 or -1 with equal probability. $S_{\boldsymbol{\pi}}$ can be written as

$$S_{\boldsymbol{\pi}} = \left|\sum_n e^{i\boldsymbol{\pi}\cdot\boldsymbol{R}_n}\frac{2\langle\sigma_z\rangle_n}{\sqrt{N}}\right|^2,$$

which is equivalent to the square of the distance travelled on an unbiased random walk with step size $1/\sqrt{N}$. The mean and standard deviation can then be readily calculated: $\overline{S_{\boldsymbol{\pi}}} = 1$ and $\sqrt{\text{Var}(S_{\boldsymbol{\pi}})} = \sqrt{2}$, where $\text{Var}(S_{\boldsymbol{\pi}})$ denotes the variance of the random variable $S_{\boldsymbol{\pi}}$. With a standard deviation that is larger than the mean value, a considerable number of shots needs to be taken in order to obtain an acceptable error in the mean. The standard error of the mean for 40 shots will be $\sqrt{2/40} = 0.22$, consistent with what we obtain in the experiment (see Fig. 4).

Numerical calculations.

DQMC and NLCE calculations are used to obtain the local values of the thermodynamic quantities in our trap, including the density, entropy, and the spin structure factor. DQMC calculations for arbitrary chemical potential (and hence density) can be obtained reliably down to temperatures slightly above the Néel temperature for a given $U/t \lesssim 9$. For stronger interactions intermediate values of n become inaccessible to DQMC due to the sign problem, in which case we rely on the NLCE to obtain values of the thermodynamic quantities for arbitrary chemical potential down to temperatures as low as $T/t = 0.40$.

DQMC results for a 6×6×6 lattice were obtained with the methodology described in Refs. [7] and [32]. Inverse

temperature discretisation $\Delta\tau = \beta/L = 1/20t$ is sufficiently small that Trotter corrections are substantially less than statistical error bars. Finite size effects were assessed by comparing DQMC results for 6×6×6 and 8×8×8 lattices. Differences are only appreciable when the spin structure factor per lattice site, $s_{\boldsymbol{\pi}} > 5$. The local value of $s_{\boldsymbol{\pi}}$ is always less than 4 in our calculations, so DQMC results in a 6×6×6 lattice are sufficient for the comparison with theory.

In NLCEs, an extensive property of the lattice model per site in the thermodynamic limit is expressed in terms of contributions from finite clusters that can be embedded in the lattice. NLCEs use the same basis as high-temperature expansions, however, properties of clusters are calculated via exact diagonalisation, as opposed to a perturbative expansion in powers of the inverse temperature [8, 33]. The site-based NLCE for the Hubbard model [34] is implemented here for a three-dimensional lattice and carried out to the eighth order for all thermodynamic quantities, except for $S_{\boldsymbol{\theta}}$, where due to the reduced symmetry, only seven orders were obtained. Within its region of convergence ($T/t \gtrsim 1.5$ for any n and U), NLCE results do not contain any systematic or statistical errors. The convergence region extends to significantly lower T/t at $n = 1$ and generally improves by increasing the interaction strength. At lower T/t, we take advantage of numerical resummations, such as Euler and Wynn transformations [33], to obtain an estimate. The NLCE provides a fast tool, which, given the value of U/t, generates results on a dense temperature and chemical potential grid in a single run.

Local density approximation.

The local density approximation, which has been previously shown to agree well with *ab initio* DQMC simulations of the trapped Hubbard Hamiltonian [35], was used to calculate the trap profiles of the different thermodynamic quantities. The spin structure factor $S_{\boldsymbol{Q}}$ is obtained from the trap profile of the spin structure factor per lattice site as

$$S_{\boldsymbol{Q}} = \frac{1}{Na^3} \int s_{\boldsymbol{\pi}} \, \mathrm{d}^3 r.$$

For the numerical calculations we set T and μ_0; local values of U/t, T/t, and the local chemical potential μ/t are calculated using the known trap potential. The local values of the thermodynamic quantities are then obtained by interpolation from NLCE and DQMC results for a homogeneous system calculated in a ($U/t, T/t, \mu/t$) grid. Radial profiles for the local value of U/t, T/t, and μ/t along a body diagonal of the lattice were used and spherical symmetry assumed.

Entropy

In Fig. 4 of the paper we compare the experimental results at various U_0/t_0 with calculations at constant T. Since ultracold atoms are isolated systems, a constant value of the overall entropy per particle $S/(Nk_{\mathrm{B}})$ may be more appropriate. We find that over the range $10 < U_0/t_0 < 15$, where AFM correlations are largest, $S/(Nk_{\mathrm{B}})$ does not vary significantly with U_0/t_0, at constant T (Extended Data Fig. 6). This implies that we do not expect significant adiabatic cooling for stronger interactions [18, 27], and thus the curves at constant T are suitable to describe the experimental data.

[31] D. A. Butts and D. S. Rokhsar, Phys. Rev. A **55**, 4346 (1997).

[32] T. Paiva, R. Scalettar, M. Randeria, and N. Trivedi, Phys. Rev. Lett. **104**, 066406 (2010).

[33] B. Tang, E. Khatami, and M. Rigol, Computer Physics Communications **184**, 557 (2013).

[34] E. Khatami and M. Rigol, Phys. Rev. A **84**, 053611 (2011).

[35] S. Chiesa, C. N. Varney, M. Rigol, and R. T. Scalettar, Phys. Rev. Lett. **106**, 035301 (2011).
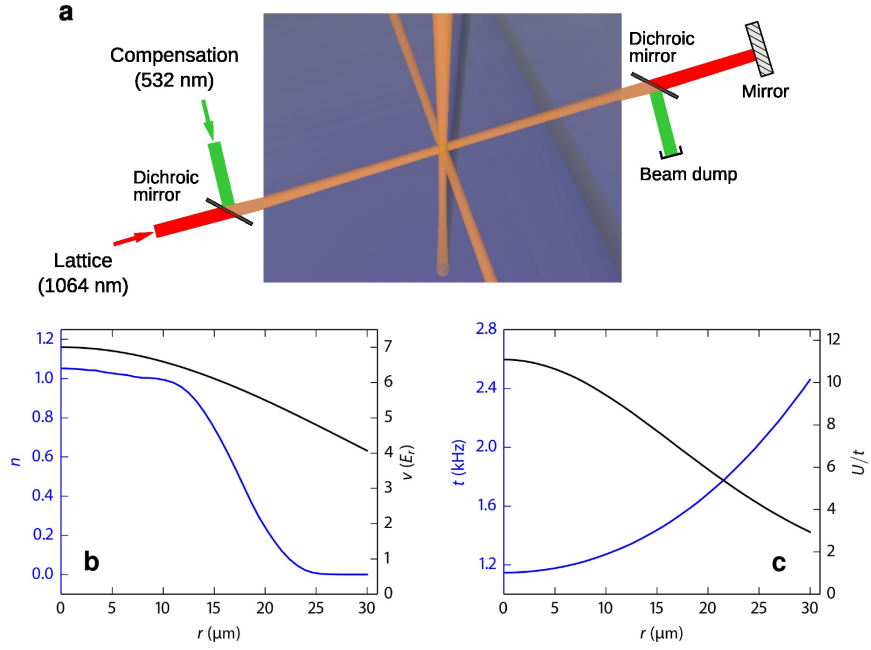
EXTENDED DATA FIG. 1. **Compensated optical lattice. a**, Schematic of the compensated optical lattice setup. Along each axis, the radial confinement of the lattice is compensated with a repulsive compensation beam which copropagates with the lattice beam but is not retroreflected. **b**, The local value of the lattice depth v (black line) is shown as a function of distance from the centre along a body diagonal of the lattice. Due to the finite extent of the lattice beams, v varies across the density profile of the cloud (blue line), which here is calculated for $U_0/t_0 = 11.1$ at $T/t_0 = 0.60$. **c**, The inhomogeneity in v results in spatially varying Hubbard parameters t (blue line) and U/t (black line).
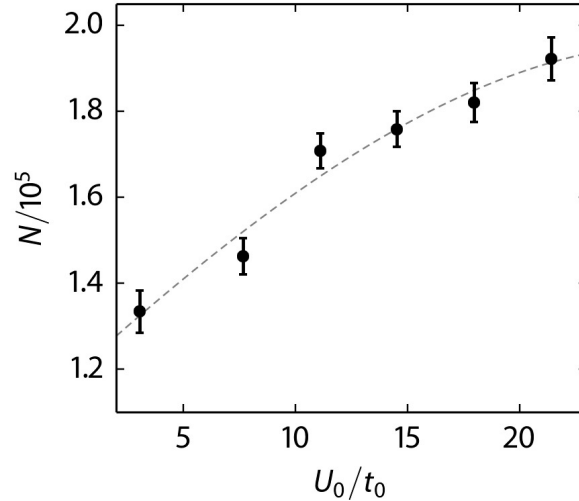

EXTENDED DATA FIG. 2. **Atom number for the data in Fig. 4.** Atom number N which maximises S_π as a function of U_0/t_0. We control N by adjusting the depth of the dimple trap. Using a linear calibration between the depth of the dimple trap and the final atom number, we obtain the value of N corresponding to the data in Fig. 4. The error bars correspond to the s.e.m of the dimple depths used in at least 40 *in-situ* and 40 time-of-flight realisations of the experiment, corresponding to the data in Fig. 4. The line is a third order polynomial fit, which is used to interpolate the value of N for numerical calculations shown in Fig. 4.
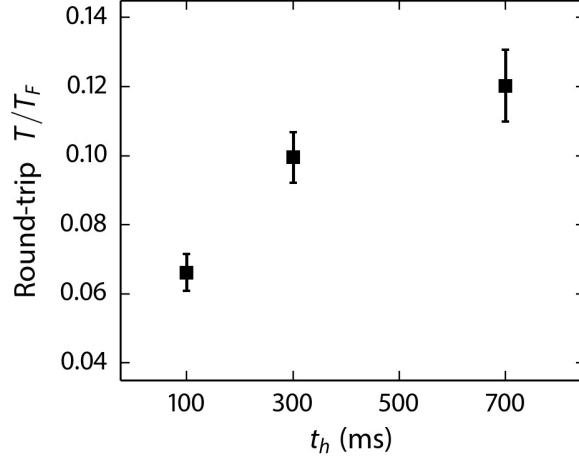
EXTENDED DATA FIG. 3. **Round-trip temperature measurements.** Measurement of the round-trip T/T_F vs. hold time t_h in a compensated lattice with $v_0 = 7\,E_r$ and $g_0 = 3.7\,E_r$. The duration of the loading ramps is not included in t_h. The scattering length is $326\,a_0$, which corresponds to $U_0/t_0 = 12.5$. Error bars are the s.e.m. of 6 independent realisations. The temperature in the dimple trap before loading into the lattice is $T/T_F = 0.04 \pm 0.02$.
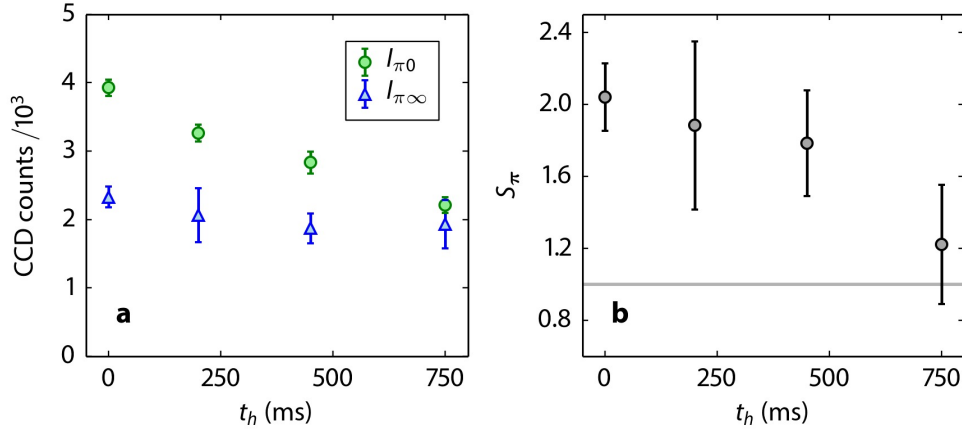
EXTENDED DATA FIG. 4. **Bragg signal decay with hold time. a**, Detected counts vs. t_h, measured for momentum transfer $\boldsymbol{Q} = \boldsymbol{\pi}$ for an *in-situ* sample ($I_{\pi0}$, green circles) and after decay of the Debye-Waller factor ($I_{\pi\infty}$, blue triangles). For longer hold times, the Bragg scattered intensity $I_{\pi0}$ decays to match $I_{\pi\infty}$, reflecting the absence of AFM correlations in a sample at higher T. **b**, The spin structure factor corresponding to the scattered intensities shown in **a**. For these measurements the scattering length is $200\,a_0$, corresponding to $U_0/t_0 = 7.7$ in a $7\,E_r$ deep lattice. The compensation is $g_0 = 4.05\,E_r$, different from that used for the data in Fig. 4. The increased compensation requires a larger atom number to realise an $n \simeq 1$ shell in the cloud. The atom number used here is 2.6×10^5 atoms. The duration of the Bragg probe is $2.7\,\mu$s for these data. Error bars in **a** are the s.e.m. of at least 5 measurements for $I_{\pi\infty}$ and at least 10 measurements for $I_{\pi0}$. Error bars in **b** are obtained from the s.e.m. of the measured intensities and equation (2).
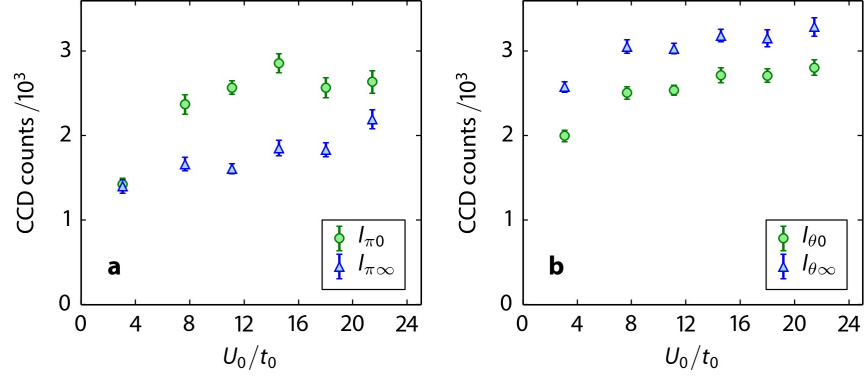
EXTENDED DATA FIG. 5. **Detected counts for measurement of spin structure factor in Fig. 4. a**, Detected counts vs. U_0/t_0, measured for momentum transfer $\boldsymbol{Q} = \boldsymbol{\pi}$ for an *in-situ* sample ($I_{\boldsymbol{\pi}0}$, green circles), and after decay of the Debye-Waller factor, ($I_{\boldsymbol{\pi}\infty}$, blue triangles). As U_0/t_0 increases we use a larger atom number to optimise the Bragg signal. $I_{\boldsymbol{\pi}\infty}$ and $I_{\boldsymbol{\pi}0}$ both increase with U_0/t_0 due to the larger N, but $I_{\boldsymbol{\pi}0}$ shows an additional enhancement due to the presence of AFM correlations. **b**, Detected counts vs. U_0/t_0, measured for momentum transfer $\boldsymbol{Q} = \boldsymbol{\theta}$ for an *in-situ* sample ($I_{\boldsymbol{\theta}0}$, green circles), and after decay of the Debye-Waller factor ($I_{\boldsymbol{\theta}\infty}$, blue triangles). For $\boldsymbol{Q} = \boldsymbol{\theta}$ most of the dependence for both the *in-situ* and time-of-flight intensities is due to the changing N. Error bars in both **a** and **b** are the s.e.m. of at least 40 measurements. The overall count rate is higher for $\boldsymbol{Q} = \boldsymbol{\theta}$ due to the different collection efficiency and gain settings of the CCD camera.
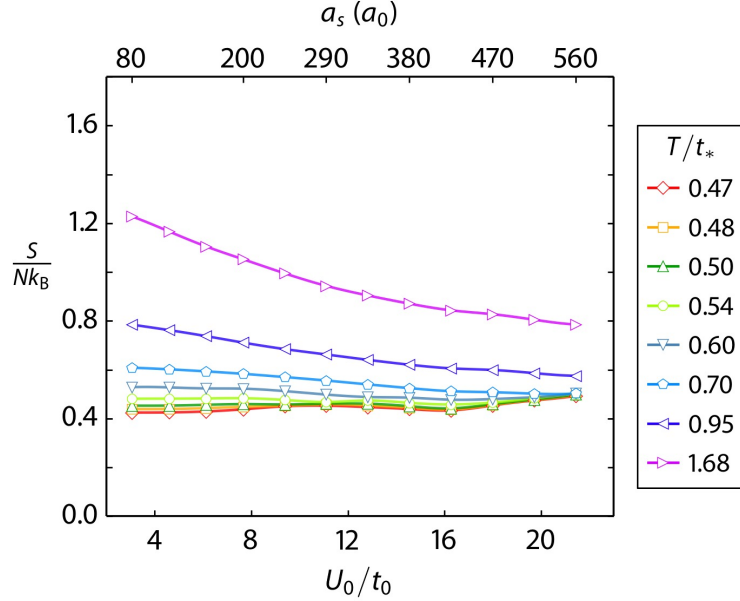
EXTENDED DATA FIG. 6. **Entropy per particle at constant T.** Overall entropy per particle $S/(Nk_{\mathrm{B}})$ as a function of U_0/t_0 for the calculations at various T/t_* shown in Fig. 4 (lines are guides to the eye). For the lowest temperatures, $S/(Nk_{\mathrm{B}})$ does not vary significantly over the range of U_0/t_0 covered by the experiment justifying the treatment at constant T. A value of $S/(Nk_{\mathrm{B}}) \simeq 0.43$ is obtained for the temperature determined from the data in Fig. 4. This entropy is consistent with $T/T_F \simeq 0.04$, measured in the harmonic dimple trap before loading the atoms into the lattice.